Chinese Chemical Letters 37 (2026) 112638

Contents lists available at ScienceDirect

Chinese Chemical Letters

journal homepage: www.elsevier.com/locate/cclet

Cu/Ni dual-atom catalysts with charge regulation: Boosting CO_2 electroreduction selectivity *via* site-specific O/C-terminal asymmetric adsorption

Jielian Yang[a], Yue Shen[a], Bing Chen[a], Qi Wu[a], Yuemei Liao[a], Liya Zhou[a,*], Jing Luo[a], Xue Mao[a], Jin Guo[a], Binbin Luo[a], Qi Pang[a], Chunyan Zhou[b], Peican Chen[a,*], Anxiang Guan[a,*]

[a] *School of Chemistry and Chemical Engineering, State Key Laboratory of Featured Metal Materials and Life-cycle Safety for Composite Structures, Guangxi Key Laboratory of Electrochemical Energy Materials, Guangxi Colleges and Universities Key Laboratory of Applied Chemistry Technology and Resource Development. Guangxi University, Nanning 530004, China*

[b] *College of Pharmaceutical Science, Guangxi Medical University, Nanning 530021, China*

ARTICLE INFO

Article history:
Received 26 January 2026
Revised 11 March 2026
Accepted 16 March 2026
Available online 17 March 2026

Keywords:
Cu/Ni dual-atom catalysts
Intermetallic interactions
CO_2 reduction
O-terminal adsorption
C-terminal adsorption

ABSTRACT

Dual-atom catalysts (DACs) show great potential for boosting reaction kinetics and diversifying active sites *via* the synergistic effects of two metal atoms. However, the influence of intermetallic interactions on catalytic performance remains underexplored. Herein, we report a Cu/Ni dual-atom catalyst anchored on N-doped carbon (Cu/Ni-N-C) for the electrochemical CO_2 reduction reaction (CO_2RR). Advanced experimental and theoretical approaches, including X-ray absorption fine structure (XAFS) analysis and density functional theory (DFT) calculations, were employed to systematically investigate the mechanism of intermetallic interactions. Experimental results demonstrate that the monometallic Cu-N-C catalyst achieves a maximum CO Faradaic efficiency (FE) of 38.35 % at -1 V *vs.* RHE, with a non-negligible CH_4 FE of 21.89 % at -1.4 V *vs.* RHE. In contrast, the $Cu_{0.5}Ni_{0.5}$–N-C catalyst exhibits significantly enhanced performance for CO formation, reaching a high CO FE of 96.78 % with partial current density of 24.80 mA/cm^2 and a negligible CH_4 formation. The reason for this selectivity shift is that Ni atoms within the Cu-Ni diatomic pairs in the Cu/Ni-N-C catalyst attract the electron cloud of Cu atoms. This reduces the electron cloud density near Cu atoms, and thus weakens the adsorption of CO_2RR intermediates on Cu sites. DFT calculations further reveal that charge regulation between Cu and Ni is the key to the improved CO selectivity: electron-deficient Cu atoms act as O-terminal adsorption sites to bind the oxygen atoms of CO_2, while electron-enriched Ni atoms serve as C-terminal adsorption sites to anchor the carbon atoms. This asymmetric adsorption mode promotes CO_2 polarization and activation, narrows the HOMO-LUMO band gap for efficient electron transfer, and reduces the thermodynamic barrier for *COOH intermediate formation ($\Delta G = 1.78$ eV *vs.* 2.52 eV for Cu-N-C). Additionally, the shortened Ni-C bond (1.921 Å *vs.* 2.207 Å for Cu-N-C) and elongated C–OH bond (1.388 Å *vs.* 1.376 Å for Cu-N-C) in *COOH on $Cu_{0.5}Ni_{0.5}$–N-C further favor CO generation. This work provides new insights into the precise design of DACs by regulating intermetallic interactions, advancing their industrial applications in CO_2RR.

© 2026 Published by Elsevier B.V. on behalf of Chinese Chemical Society and Institute of Materia Medica, Chinese Academy of Medical Sciences.

With atmospheric CO_2 concentrations in the atmosphere reaching unacceptably high levels and continuing to rise, capturing atmospheric CO_2 and converting it into value-added fuels has become both essential and sustainable [1–3]. The electrochemical CO_2 reduction reaction (CO_2RR) stands out as an effective and promising strategy for transforming CO_2 into high-value chemicals and liquid fuels [4]. Among the various products of electrochemical CO_2RR, CO serves as a fundamental feedstock for methanol synthesis, Fischer-Tropsch synthetic oils, and diverse carbonylation reactions [5]. However, this conversion process involves two proton-coupled electron transfer steps, posing challenges such as identifying active sites and competing with the hydrogen evolution reaction (HER) [6–8]. In recent years, single-atom catalysts (SACs) have attracted significant attention due to their well-defined active sites and excellent selectivity for C_1 products [6,9–11].

* Corresponding authors.
E-mail addresses: zhouliya@gxu.edu.cn (L. Zhou), peicanchen@gxu.edu.cn (P. Chen), Axguan24@gxu.edu.cn (A. Guan).

https://doi.org/10.1016/j.cclet.2026.112638
1001-8417/© 2026 Published by Elsevier B.V. on behalf of Chinese Chemical Society and Institute of Materia Medica, Chinese Academy of Medical Sciences.

Carbon-based SACs play a pivotal role in electrocatalysis due to their versatile structures, exceptional stability, and high conductivity [12–14]. Their high activity in CO_2RR systems is typically associated with symmetric M-N_4 sites, such as Cu-N_4 [15], Ni-N_4 [16], or Co-N_4 [17]; yet, challenges regarding activity, stability, and product selectivity persist. For instance, excessively strong *CO adsorption energy or a high *COOH energy barrier can result in unsatisfactory selectivity and stability [18,19]. To address these issues, dual-atom catalysts (DACs) with diverse metal combinations have been developed, leveraging interactions between the two metals to effectively lower reaction barriers, accelerate reaction rates, and thus achieve superior catalytic performance [20–22]. However, to the best of our knowledge, recent research has predominantly focused on comparing DACs with SACs, with limited studies investigating how intermetallic interactions influence CO_2RR performance in DACs systems [23,24].

This study explores the impact of intermetallic interactions on the CO_2RR performance of Cu/Ni-NC DACs. Theoretical simulations were conducted on Cu/Ni-NC DACs models to assess how intermetallic interactions affect electronic structure, CO_2RR activity, and selectivity, ultimately identifying the reason for the selectivity shift in Cu-N-C catalysts after Ni doping. These findings highlight that intermetallic interactions are a critical and reliable parameter influencing catalytic activity in DACs systems. Aberration-corrected high-angle annular dark-field scanning transmission electron microscopy (AC–HAADF-STEM) and X-ray absorption fine structure (XAFS) analyses further confirmed that the synthesized Cu/Ni-N-C catalyst features an atomic configuration with neighboring Cu/Ni sites coordinated with four nitrogen atoms, respectively. The resulting catalyst efficiently facilitates the selective conversion of CO_2 to CO, achieving nearly 100 % CO Faradaic efficiency (FE_{CO}) at −1.3 V *vs.* RHE in an H-type cell. Density functional theory (DFT) calculations reveal that the Cu/Ni dual-atom catalyst synergistically electroreduces CO_2 to CO: The Cu atom, with low charge density, adsorbs the oxygen atom of the CO_2 molecule; while the Ni atom, with high charge density, adsorbs the carbon atom of the CO_2 molecule, collectively enhancing overall CO_2RR activity. This study underscores the importance of tuning intermetallic interactions in DACs to maximize synergistic effects and optimize CO_2RR performance.

The fabrication of Cu-Ni dual-atom catalysts is schematically illustrated in Fig. 1. 1,3,5-Benzenetricarboxylic acid, copper(II) nitrate trihydrate, and PVP were used as starting materials to synthesize HKUST-1 metal-organic framework (MOF) *via* a hydrothermal reaction (see Experimental Section in Supporting information). When copper(II) nitrate trihydrate was partially substituted with nickel nitrate hexahydrate, with all other experimental procedures kept unchanged, (CuNi)HKUST-1 MOFs with different Cu/Ni ratios were successfully obtained. The crystal phase and morphology of the as-synthesized samples were characterized by X-ray diffraction (XRD, Fig. S1 in Supporting information) and scanning electron microscopy (SEM, Figs. 2a-c and Fig. S2 in Supporting information). Results confirmed the successful synthesis of HKUST-1 MOF and showed no changes in the structure or morphology of HKUST-1 after partial substitution of Cu atoms with Ni atoms. Finally, HKUST-1 and (Cu_xNi_y)HKUST-1 MOFs were mixed with dicyandiamide and then calcined; the resulting products were designated as Cu_xNi_y-N-C-BL (where x:y = 1:0, 0.8:0.2, 0.5:0.5 and 0:1; BL means before acid leaching). After acid leaching under an oxygen atmosphere, metal particles in the Cu_xNi_y-N-C-BL samples were removed, yielding target products of Cu_xNi_y-N-C. For comparison, nitrogen-doped carbon (N–C) was also synthesized without adding any metal components.

Scanning electron microscopy (SEM) images show that all Cu_xNi_y-N-C-BL samples consist of interconnected foam structures with wrinkled, entangled flakes (Fig. S7 in Supporting information), which is similar to the Cu-N-C sample (Fig. 2e). The low-resolution transmission electron microscopy (TEM) image of the Cu-N-C catalyst reveals cross-linked, ultrathin folded-sheet features (Fig. 2f) and the corresponding high-resolution TEM (HRTEM) image confirms no observable copper particles in the Cu-N-C catalyst (Fig. 2g). The selected-area electron diffraction (SAED) pattern (inset of Fig. 2g) further confirms the sample's non-crystalline nature. Energy-dispersive spectroscopy (EDS) elemental mapping shows the existence of Cu, N, and C elements and the uniform distribution of N and Cu across the entire carbon matrix (Fig. 2h). As presented in Figs. 2i-k and Figs. S8-S11 (Supporting information), the $Cu_{0.5}Ni_{0.5}$–N-C, $Cu_{0.8}Ni_{0.2}$–N-C and Ni-N-C samples display a morphology analogous to that of the Cu-N-C sample, with no distinct metal particles observed on their surfaces. EDS elemental mapping further verifies the homogeneous distribution of N, Cu, and Ni across the carbon support (Figs. 2l-m and Figs. S9-S11). As illustrated in the AC–HAADF-STEM image (Fig. 2n), numerous bright spot pairs are distinctly observed, which are indicative of potential atomic-scale active sites. Furthermore, the 3D surface plot derived from region 1 of Fig. 2n offers compelling evidence to corroborate the existence and structural features of these atomic pairs (Fig. 2o). In addition, statistical analysis presented in Fig. 2p clearly demonstrates that over 88.73 % of the detected sites correspond to isolated dual-atom configurations (circled with red dashed lines) with a distance around 2.81–2.92 Å (Fig. 2q). The electron energy-loss spectroscopy (EELS) diagram in Fig. S12 (Supporting information) further confirmed the co-existence of Ni and Cu atomic pairs. The small interatomic distance between Cu and Ni induces intense through-space and through-bond electronic coupling interactions, effectively expediting the migration of electrons between Cu and Ni. Collectively, these characterizations confirm that Cu/Ni dual-atom sites are not only the dominant active species but also uniformly distributed throughout the $Cu_{0.5}Ni_{0.5}$–N-C samples, laying a solid foundation for their enhanced catalytic performance. The Raman spectra of Cu-N-C, $Cu_{0.8}Ni_{0.2}$–N-C, and $Cu_{0.5}Ni_{0.5}$–N-C samples exhibit two prominent characteristic peaks at approximately 1355 and 1570 cm^{-1} (Fig. S13 in Supporting information), which are ascribed to the d-band and G-band, respec-

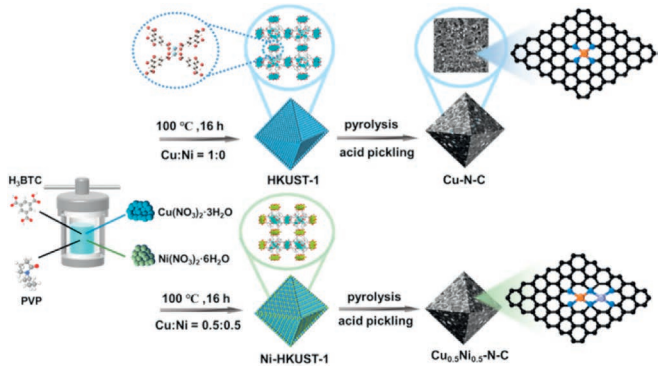


Fig. 1. Schematic of the procedure to synthesize Cu-N-C and $Cu_{0.5}Ni_{0.5}$–N-C catalysts. Orange sphere: Cu atom, purple sphere: Ni atom, blue sphere: N atom, black sphere: C atom.The XRD patterns of all Cu_xNi_y-N-C-BL samples exhibit sharp diffraction peaks at $2\theta = 43.3°$, 50.4°, and 74.1° (Fig. 2d, Figs. S3 and S4 in Supporting information), corresponding to the (111), (200), and (220) crystal planes of the cubic Cu structure (JCPDS No. 04–0836). After acid leaching, the resulting Cu_xNi_y-N-C samples show only a broad peak centered at 26.4°, which is attributed to the (002) plane of the hexagonal graphitic structure (Fig. 2d and Figs. S3-S5 in Supporting information) and confirms the complete removal of metallic Cu *via* acid leaching. This is because metal particles had weak interactions with the carbon matrix and were thus dissolved in the oxygen-saturated acid solution. For comparison, the XRD pattern of the nitrogen-doped carbon (N–C) sample was also examined (Fig. S6 in Supporting information), where no Cu diffraction peaks are observed and only the carbon-related peak is identifiable.

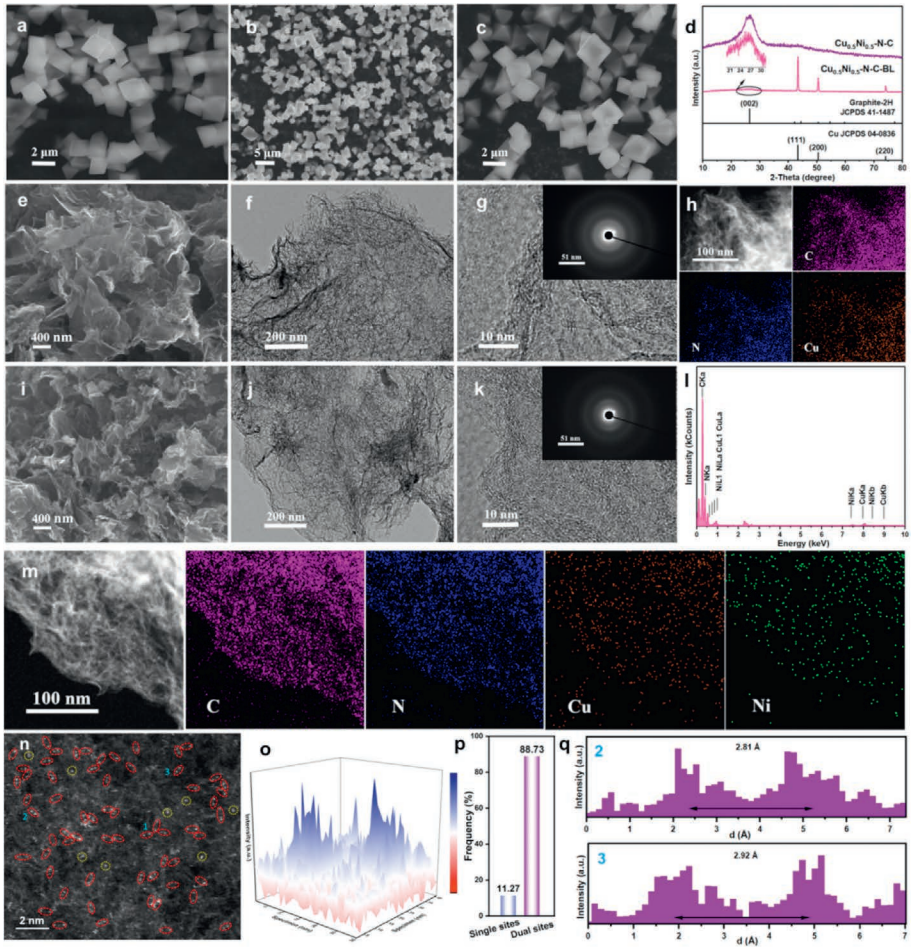


Fig. 2. (a) High-magnification SEM image of HKUST-1. (b) Low-magnification SEM image of ($Cu_{0.5}Ni_{0.5}$) HKUST-1 MOF. (c) High-magnification SEM image of ($Cu_{0.5}Ni_{0.5}$) HKUST-1 MOF. (d) XRD patterns of $Cu_{0.5}Ni_{0.5}$–N-C-BL and $Cu_{0.5}Ni_{0.5}$–N-C samples. (e) SEM image of Cu-N-C. (f) Low-magnification TEM image of Cu-N-C. (g) High-magnification TEM image of Cu-N-C, with the inset showing the corresponding selected area electron diffraction pattern. (h) EDS elemental distribution map of Cu-N-C. (i) SEM image of $Cu_{0.5}Ni_{0.5}$–N-C. (j) Low-magnification TEM image of $Cu_{0.5}Ni_{0.5}$–N-C. (k) High-magnification TEM image of $Cu_{0.5}Ni_{0.5}$–N-C, with the inset showing the corresponding selected area electron diffraction pattern. (l) EDS analysis of $Cu_{0.5}Ni_{0.5}$–N-C. (m) EDS elemental distribution map of $Cu_{0.5}Ni_{0.5}$–N-C. (n) AC–HAADF-STEM image of $Cu_{0.5}Ni_{0.5}$–N-C (dual-atom sites (circled in red) and single-atom sites (circled in yellow)). (o) 3D surface plot from region 1 of (n). (p) Statistical distribution of single sites and dual sites in $Cu_{0.5}Ni_{0.5}$–N-C. (q) Intensity profiles obtained from areas 2–3 in (n).

tively [25,26]. Defect concentrations were quantified by normalizing the intensity of the d-band relative to that of the G-band (*i.e.*, the I_D/I_G ratio, Table S1 in Supporting information) [25]. Notably, the I_D/I_G values were calculated as 1.09, 1.08 and 1.07 for Cu-N-C, $Cu_{0.5}Ni_{0.5}$–N-C and $Cu_{0.8}Ni_{0.2}$–N-C samples, respectively, which are comparable and indicate that the defect content in these Cu_xNi_y-N-C samples is not the critical factor governing their catalytic performance. N_2 adsorption-desorption isotherms and corresponding pore size distribution analyses (Fig. S14 in Supporting information) confirm that all samples share comparable Brunauer-Emmett-Teller (BET) specific surface areas and total pore volumes. For example, the $Cu_{0.5}Ni_{0.5}$–N-C sample achieves a BET specific surface area of 137.71 m^2/g and a total pore volume of 0.62 cm^3/g, which is similar to that of the Cu-N-C and Ni-N-C sample. Such favorable textural characteristics are capable of optimizing the mass transfer behavior of CO_2 and electrolyte at the triple-phase interface, thereby creating favorable conditions for the smooth progression of the CO_2 electroreduction reaction.

X-ray photoelectron spectroscopy (XPS) measurements were conducted to systematically investigate the chemical composition and elemental valence states of the Cu_xNi_y-N-C and Cu-N-C samples. As revealed by the XPS survey spectra (Fig. S15 in Supporting information), Cu_xNi_y-N-C contained four main elements, *i.e.*, C, N, Cu and Ni, confirming the successful incorporation of N, Cu and Ni into the carbon sheet matrix. Notably, the N dopant is inherently derived from the dicyandiamide precursor. As shown in Fig. S16 (Supporting information), the high-resolution C 1s spectrum of the $Cu_{0.5}Ni_{0.5}$–N-C sample deconvolutes into four major peaks centered at 284.6, 286, 287.3 and 289.1 eV, which correspond to sp^2-bonded C=C, sp^3-bonded C–N, C–O, and C=O functional groups, respectively [27]. Fig. 3a presents the high-resolution N 1s XPS spectrum of $Cu_{0.5}Ni_{0.5}$–N-C, revealing five distinct sub-peaks at 398.7, 399.2, 400.1, 401.1 and 403.1 eV. These peaks are assigned to pyridinic N, Cu/Ni-N_x, pyrrolic N, graphitic N, and oxidized N, respectively. The presence of the Cu/Ni-N_x peak in the deconvoluted N 1s spectrum provides direct evidence for the formation of Cu/Ni-N_x coordination groups in the sample [27–29]. For the Cu 2p region (Fig. 3b), the peaks at 932.50 and 934.8 eV are attributed to the $2p_{3/2}$ orbitals of Cu(I) and Cu(II) species, while those at 952.2 and 954.7 eV correspond to the $2p_{1/2}$ orbitals of Cu(I) and Cu(II), respectively. Additional satellite peaks at 942.8 and 944.9 eV further confirm the presence of Cu oxide phases in the carbon matrix, which is further confirmed by the Cu Auger spectra in Fig. S17 (Supporting information) [27,30]. In the high-resolution Ni 2p spectrum of $Cu_{0.5}Ni_{0.5}$–N-C (Fig. 3c), the peaks at 855.29 and 872.78 eV are assigned to Ni $2p_{3/2}$ and Ni $2p_{1/2}$, respectively. The absence of the

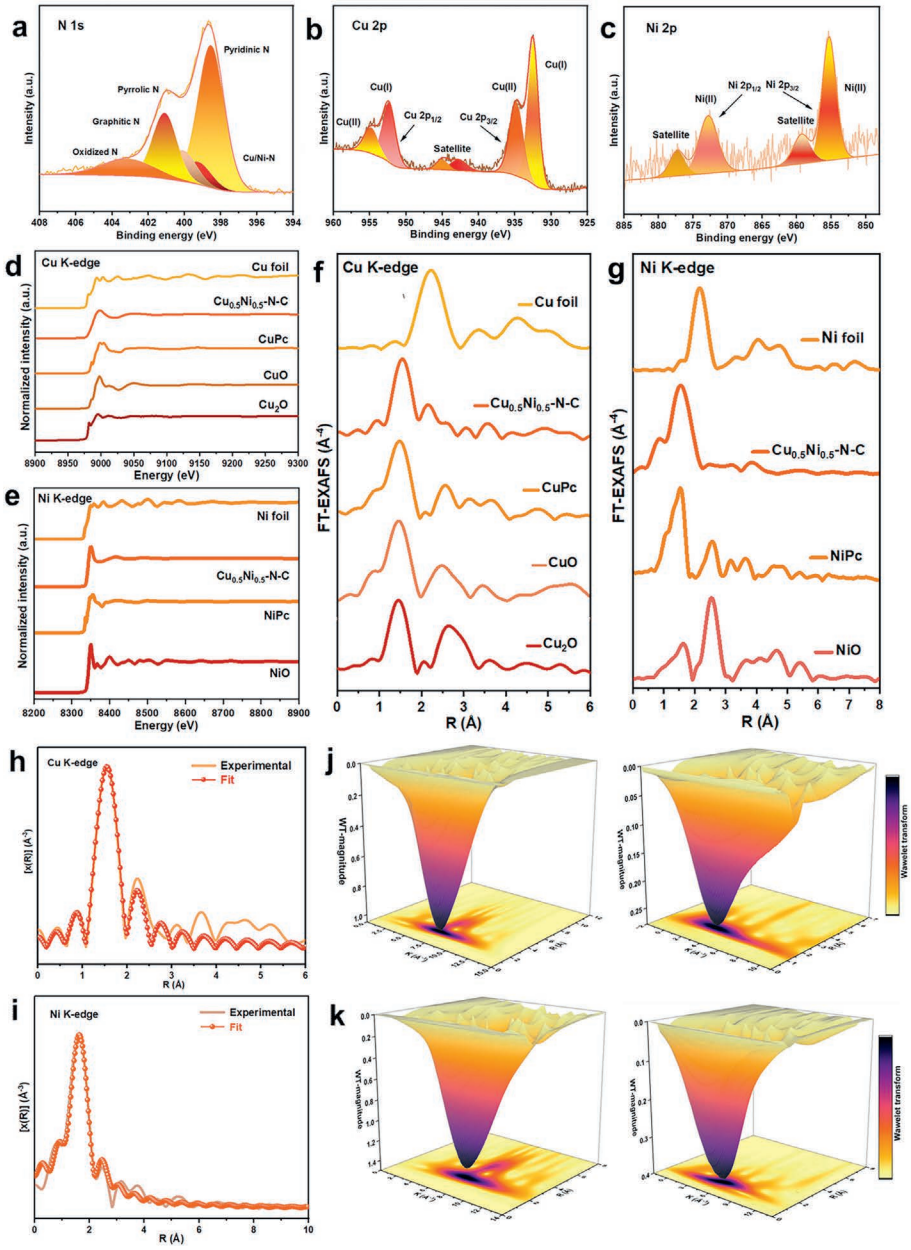


Fig. 3. High-resolution (a) N 1s, (b) Cu 2p, and (c) Ni 2p XPS spectra of $Cu_{0.5}Ni_{0.5}$–N-C. (d) Cu K-edge and (e) Ni K-edge XANES spectra of $Cu_{0.5}Ni_{0.5}$–N-C. FT-EXAFS spectra of (f) Cu K-edge and (g) Ni K-edge of $Cu_{0.5}Ni_{0.5}$–N-C. (h) EXAFS fitting of $Cu_{0.5}Ni_{0.5}$–N-C in the R space at the Cu K-edge and (i) Ni K-edge of $Cu_{0.5}Ni_{0.5}$–N-C. (j) Wavelet transform images of EXAFS data at Cu K-edge with the optimized Morlet parameter for CuPc (left) and $Cu_{0.5}Ni_{0.5}$–N-C (right). (k) Wavelet transform images of EXAFS data at Ni K-edge with the optimized Morlet parameter for NiPc (left) and $Cu_{0.5}Ni_{0.5}$–N-C (right).

metallic Ni $2p_{3/2}$ peak (at 852.6 eV) indicates that the dispersed Ni species observed in HAADF-STEM images exist as Ni^{+} or Ni^{2+} cations [31]. For comparison, XPS measurements were conducted on Cu-N-C, Ni-N-C and $Cu_{0.8}Ni_{0.2}$–N-C under the same conditions (Figs. S18-S20 in Supporting information). The results indicated that the chemical states of the major elements are analogous to those of $Cu_{0.5}Ni_{0.5}$–N-C. Notably, the divergent orbital hybridization behaviors and electron-donating properties of Cu and Ni in their N-coordination interactions trigger an asymmetric charge redistribution in the Cu-Ni diatomic pair. As observed, the binding energy of Cu $2p_{3/2}$ in Cu-N-C is 932.35 eV, and that of Ni $2p_{3/2}$ in Ni-N-C is 855.47 eV. While the Cu $2p_{3/2}$ binding energy in $Cu_{0.5}Ni_{0.5}$–N-C shifts to 932.50 eV (an increase of 0.15 eV), and the Ni $2p_{3/2}$ binding energy shifts to 855.29 eV (a decrease of 0.18 eV) (Fig. S21 in Supporting information). These shifts directly confirm the proposed electron transfer from Cu to Ni in the dual-atom catalyst.

X-ray absorption near-edge spectroscopy (XANES) and Fourier-transformed extended X-ray absorption fine structure (FT-EXAFS) were employed to characterize the structural and electronic properties of Cu and Ni sites in the $Cu_{0.5}Ni_{0.5}$–N-C sample. As shown in Fig. 3d, the Cu K-edge XANES spectrum of the $Cu_{0.5}Ni_{0.5}$–N-C catalyst places the Cu absorption peak between those of CuPc and Cu foil, confirming the oxidized state of Cu. Similarly, Fig. 3e displays the Ni K-edge XANES spectrum of the $Cu_{0.5}Ni_{0.5}$–N-C sample, where the Ni absorption peak is positioned between those of NiO/NiPc and a Ni foil, indicating that Ni is present in an oxidized state. For the FT-EXAFS analysis, Fig. 3f displays the Cu K-edge FT-EXAFS spectrum of the $Cu_{0.5}Ni_{0.5}$–N-C sample, which is characterized by a dominant peak at 1.54 Å and can be assigned to

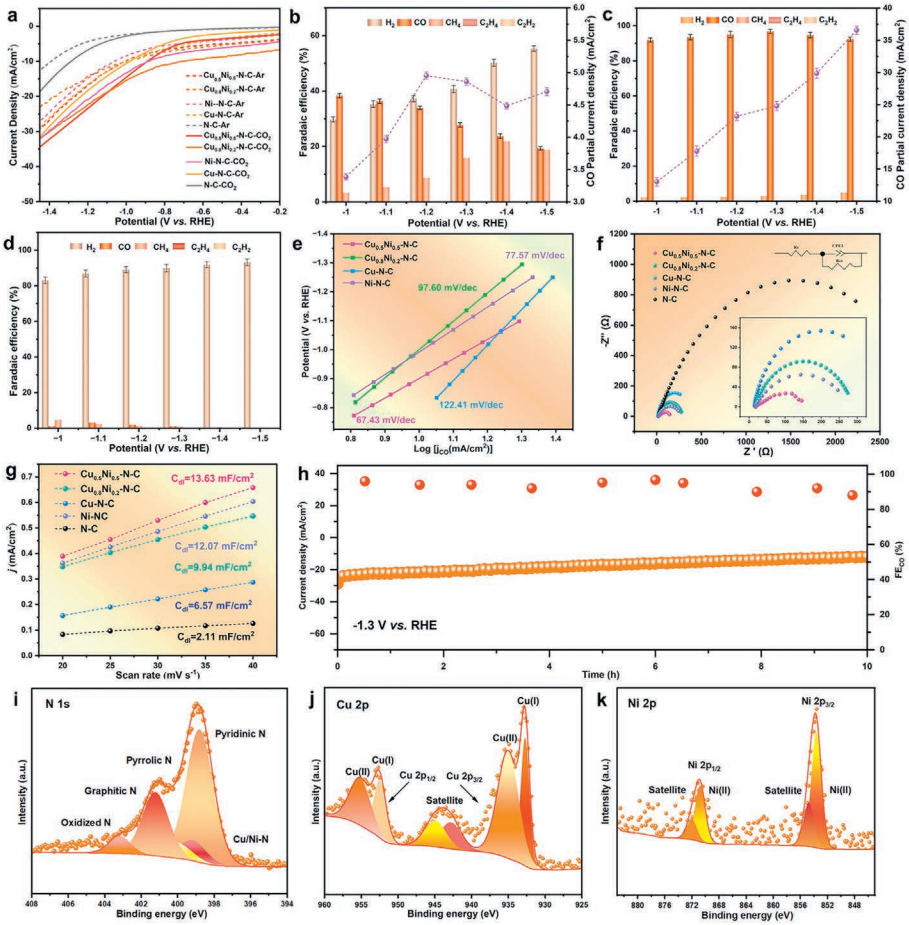


Fig. 4. (a) LSV curves of $Cu_{0.5}Ni_{0.5}$–N-C, $Cu_{0.8}Ni_{0.2}$–N-C, Cu-N-C, Ni-N-C and N–C in 0.1 mol/L $KHCO_3$ saturated with Ar or CO_2. Faradaic efficiency (FE) of all CO_2RR products at different potentials of (b) Cu-N-C, (c) $Cu_{0.5}Ni_{0.5}$–N-C, (d) N–C. (e) Tafel plots for CO_2RR over $Cu_{0.5}Ni_{0.5}$–N-C, $Cu_{0.8}Ni_{0.2}$–N-C, Cu-N-C, Ni-N-C and N–C. (f) Nyquist curves of $Cu_{0.5}Ni_{0.5}$–N-C, $Cu_{0.8}Ni_{0.2}$–N-C, Cu-N-C, Ni-N-C and N–C. (g) CV fitting curves of $Cu_{0.5}Ni_{0.5}$–N-C, $Cu_{0.8}Ni_{0.2}$–N-C, Cu-N-C, Ni-N-C and N–C. (h) Stability assessment of $Cu_{0.5}Ni_{0.5}$–N-C at −1.3 V *vs.* RHE. High-resolution (i) N 1s, (j) Cu 2p, and (k) Ni 2p XPS of $Cu_{0.5}Ni_{0.5}$–N-C catalyst after CO_2RR.

Cu-N coordination environments. Notably, a small peak positioned at 2.12 Å was observed, which is due to the weak interaction between Cu and adjacent Ni atoms. Correspondingly, the Ni K-edge FT-EXAFS spectrum (Fig. 3g) shows a major peak at 1.56 Å for the sample, associated with Ni-N bonding. To determine the detailed structural configuration of Cu and Ni in $Cu_{0.5}Ni_{0.5}$–N-C sample, the FT-EXAFS spectra were further fitted (Figs. 3h and i, Figs. S22 and S23 in Supporting information). The fitting results (Tables S2 and S3 in Supporting information) reveal that the coordination numbers (CN) of Cu-N and Ni-N in the catalyst are 4.03 and 4, respectively. Wavelet transforms (WT) were used to validate the above conclusions, as they provide resolution in both R and k space. The WT contour plots of the $Cu_{0.5}Ni_{0.5}$–N-C catalyst exhibit a strong signal at 2.68 $Å^{-1}$, which corresponds to Cu-N contributions and is consistent with the signal of CuPc (Fig. 3j and Fig. S24 in Supporting information). A comparable finding was obtained from the WT-EXAFS analysis of the Ni K-edge (Fig. 3k and Fig. S25 in Supporting information).

To evaluate the performance of Cu_xNi_y-N-C catalysts, each catalyst powder was drop-coated onto a carbon paper with a Nafion binder to fabricate the working electrode. CO_2 reduction reaction tests were conducted in a three-electrode H-cell configuration using 0.1 mol/L $KHCO_3$ aqueous electrolyte saturated with CO_2. Linear sweep voltammetry (LSV) curves were recorded for all samples in both Ar- and CO_2-saturated 0.1 mol/L $KHCO_3$ solutions. As shown in Fig. 4a, the current densities were notably higher under CO_2 atmosphere compared to Ar, indicating their strong catalytic activities toward CO_2RR. The potential-dependent gas product distribution of all samples was measured between −1 V and −1.5 V *vs.* RHE, with in-line gas chromatography (GC) used for gas product quantification. For the Cu-N-C sample, CO_2RR yielded main products including CO and CH_4 with maximum Faradaic efficiency (FE) of CO 38.35 % at −1 V *vs.* RHE and maximum FE_{CH_4} 21.89 % at −1.4 V *vs.* RHE (Fig. 4b). In contrast, $Cu_{0.8}Ni_{0.2}$–N-C and $Cu_{0.5}Ni_{0.5}$–N-C exhibited distinct catalytic selectivity. The $Cu_{0.8}Ni_{0.2}$–N-C catalyst achieved a maximum FE_{CO} of 66.69 % at −1.3 V *vs.* RHE, corresponding to a partial current density of 10.06 mA/cm^2 (Fig. S26 in Supporting information).

Interestingly, increasing the Ni content enhanced CO generation, making it the dominant product. For $Cu_{0.5}Ni_{0.5}$–N-C, the maximum FE_{CO} reached 96.78 % with a partial current density of 24.80 mA/cm^2 at −1.3 V *vs.* RHE and negligible CH_4 and liquid products were detected (Fig. 4c, Figs. S27 and S28 in Supporting information), exhibiting a different product selectivity from that of Cu-N-C catalyst. Notably, the optimal $Cu_{0.5}Ni_{0.5}$–N-C dual-atom catalyst displays a superior ability for CO formation relative to the Ni-N-C single-atom catalyst, where the latter yields a maximum FE_{CO} of 86 % at −1.3 V *vs.* RHE with a partial current density of 20.59 mA/cm^2 (Fig. S29 in Supporting information). The distinct shift in selectivity arises from the formation of Cu-Ni atomic pairs after Ni doping into the Cu-N-C catalyst. As Ni has a higher electronegativity than copper, the electron cloud density of Cu atoms is reduced, which weakens the adsorption of intermediate species

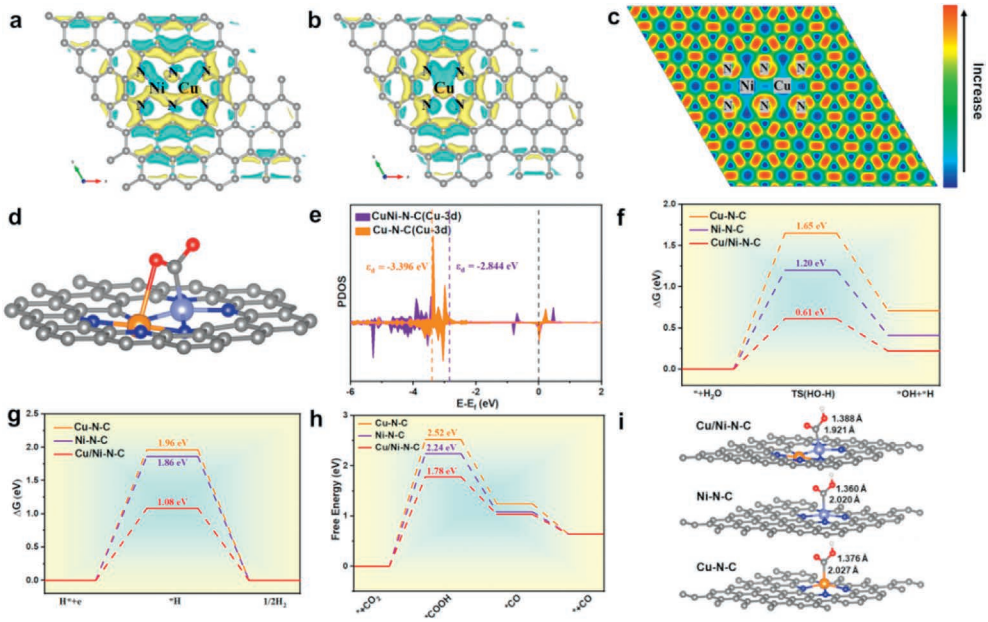


Fig. 5. (a, b) The charge density difference of Cu/Ni-N-C and Cu-N-C. The yellow and cyan region indicates electron accumulation and depletion, respectively. (c) ELF analysis for Cu/Ni-N-C with color indicating where red and blue indicate electron localization and delocalization regions, respectively. (d) Proposed CO_2 configuration adsorbed on the Cu/Ni-N-C due to the electron distribution differences between the localized positive charge on the Cu sites and negative Ni sites. (e) Projected density of states demonstrating the Cu d-states of Cu/Ni-N-C and Cu-N-C. The Fermi energy is illustrated by a black dashed line, while d-band centers (ε_d) for Cu-N-C and Cu/Ni-N-C are marked by orange and purple dashed lines, respectively. Adsorption energy diagram of (f) H_2O dissociation and (g) hydrogen ad-desorption for Cu-N-C, Ni-N-C and Cu/Ni-N-C. (h) Gibbs free energy diagrams for the formation of CO on Cu-N-C, Ni-N-C and Cu/Ni-N-C. (i) Structural comparison of COOH* adsorbed on Cu-N-C and Cu/Ni-N-C, showing atomic configurations and bond lengths. Color codes: Cu (orange), Ni (purple), N (blue), C (gray), O (red), H (white).

during the CO_2 reduction reaction. This effect hinders the subsequent protonation process of the CO_2RR intermediates (*e.g.*, *CO), thereby suppressing CH_4 formation and elevating CO selectivity. The reduced electron cloud density around Cu atoms in the Cu/Ni-N-C catalyst, in comparison with the Cu-N-C catalyst, is further verified by the calculations of charge density difference and electron localization function (Figs. 5a-c, Figs. S36 and S37 in Supporting information). For comparison, the N–C catalyst was tested and showed negligible CO_2RR activity. It exhibited nearly full Faradaic efficiency toward HER across various applied potentials (Fig. 4d). These results confirm that Ni and Cu species serve as the main active sites for CO_2RR in Cu_xNi_y-N-C catalysts. To gain deeper insight into reaction kinetics, Tafel analysis was performed as presented in Fig. 4e and the potential window adopted for Tafel fitting ranges from −0.75 V to −1.3 V *vs.* RHE. This range was chosen because FE_{CO} stays above 90 % to guarantee CO_2RR dominance, current density increases linearly with overpotential (a signature of kinetic control free of mass transfer constraints), and negligible side reactions like hydrogen evolution take place. The $Cu_{0.5}Ni_{0.5}$–N-C catalyst had a Tafel slope of 67.43 mV/dec, lower than those of Ni-N-C (77.57 mV/dec), Cu-N-C (122.41 mV/dec), and $Cu_{0.8}Ni_{0.2}$–N-C (97.60 mV/dec). This indicates that $Cu_{0.5}Ni_{0.5}$–N-C effectively promotes the first electron transfer to form the adsorbed *COOH intermediate, accelerating overall CO_2RR dynamics. Electrochemical impedance spectroscopy (EIS) measurements further validated the reaction kinetics. As shown in Fig. 4f, the R_{ct} values of N–C, Cu-N-C, Ni-N-C, $Cu_{0.8}Ni_{0.2}$–N-C, and $Cu_{0.5}Ni_{0.5}$–N-C are approximately 3055, 368.5, 265.7, 279.5 and 167.7 Ω, respectively, and the $Cu_{0.5}Ni_{0.5}$–N-C displays the smallest semicircle, which means faster electron transfer kinetics compared to the other catalysts, demonstrating efficient interfacial charge transfer.

The electrochemically active surface area (ECSA), a key factor influencing intrinsic catalytic activity, is proportional to the double-layer capacitance (C_{dl}). Cyclic voltammetry (CV) measurements were used to determine C_{dl} values for N–C, Cu-N-C, Ni-N-C, $Cu_{0.8}Ni_{0.2}$–N-C, and $Cu_{0.5}Ni_{0.5}$–N-C (Fig. S30). The calculated C_{dl} values were 2.11 mF/cm^2 (N–C), 6.57 mF/cm^2 (Cu-N-C), 12.07 mF/cm^2 (Ni-N-C), 9.94 mF/cm^2 ($Cu_{0.8}Ni_{0.2}$–N-C), and 13.63 mF/cm^2 ($Cu_{0.5}Ni_{0.5}$–N-C) (Fig. 4g). These results further support the significantly enhanced CO_2RR activity of $Cu_{0.5}Ni_{0.5}$–N-C. Furthermore, the superior intrinsic activity of $Cu_{0.5}Ni_{0.5}$–N-C is further highlighted by calculating the turnover frequency (TOF). The developed $Cu_{0.5}Ni_{0.5}$–N-C exhibits an exceptionally high TOF of 15,372 h^{-1} at −1.3 V *vs.* RHE, outperforming most of the reported state-of-the-art single atom catalysts evaluated under similar conditions (Table S4 in Supporting information). $Cu_{0.5}Ni_{0.5}$–N-C catalyst shows excellent durability with negligible decrease in current density, and FE_{CO} approximately remains about 90 % after continuous electrocatalysis for 10 h (Fig. 4h). Post-stability characterizations *via* XRD, SEM, AC–HAADF-STEM image and XPS (Figs. 4i-k and Figs. S31-S35 in Supporting information) revealed no significant changes in the catalyst's phase structure, morphology, or elemental composition, confirming its good stability. This outstanding durability is due to the strong coupling interaction of N-coordinated dual atomic sites in the carbon support. This interaction reduces *CO poisoning and accelerates CO desorption from active sites, thereby enhancing stability during CO_2RR.

To understand the origin of the enhancement in the catalytic activity of Cu/Ni-N-C catalyst, DFT calculations were conducted to analyze its electronic properties. Charge density difference (CDD) analysis reveals pronounced electron accumulation (yellow region) on Ni atoms and electron depletion (cyan region) on Cu atoms. This directly visualizes the electron density bias toward Ni and thus indicates a stronger interaction between Ni atoms and the intermediates of the electrochemical CO_2 reduction reaction (Fig. 5a). More electron accumulation around Ni active centers than around Cu atoms is also observed in both Cu-N-C and Ni-N-C configurations (Fig. 5b and Fig. S36 in Supporting information), further verifying that the catalytic activity of Ni-N sites is higher than that of Cu-N sites. This observation is further corroborated by electron lo-

calization function (ELF) analysis, which reveals localized electron density between the Cu-N and Ni-N moieties and demonstrates that Ni-N sites exhibit higher electron density than Cu-N sites (Fig. 5c and Fig. S37 in Supporting information). This electron distribution is likely to have a substantial influence on the adsorption behavior of the intermediates and the reaction selectivity. When CO_2 is polarized, its lowest unoccupied molecular orbital is concentrated mainly on the carbon atom, making it vulnerable to nucleophilic attacks. Nevertheless, the presence of regions with localized positive charge on the catalyst surface can impede nucleophilic attacks on the carbon atom. This, in turn, raises the thermodynamic barrier for *COOH adsorption. As a result, for the Cu/Ni-N-C catalyst, the carbon atom of polarized CO_2 molecules preferentially adsorbs onto the electron-enriched Ni active sites, while the oxygen atoms of CO_2 tend to bind more strongly to the electron-deficient Cu active sites (Fig. 5d). This unique adsorption mode is a direct consequence of the electron density bias toward Ni and serves as theoretical evidence for the charge transfer from Cu to Ni, which is consistent with the XPS results.

The shift from monometallic Ni-N-C and Cu-N-C to bimetallic Cu/Ni-N-C brings about remarkable alterations to the electronic structure of the catalysts. To establish how such electronic structural changes are associated with CO_2RR catalytic activity, orbital analysis was further performed in this work. As Cu/Ni-N-C delivered boosted catalytic performance with metal sites acting as the active sites, this specific configuration was prioritized for systematic investigation and compared against Cu-N-C, aiming to unravel the underlying reasons for the disparities in their catalytic behaviors. Nickel possesses a valence electron configuration of $3d^8 4s^2$, whereas copper has that of $3d^{10} 4s^1$. Within the Cu-Ni dual-atom architecture, the unoccupied 3d orbitals of Ni ($3d^8$) are able to accept electron density from the fully filled 3d orbitals of Cu ($3d^{10}$), thereby enabling orbital hybridization-driven interatomic electron transfer. PDOS calculations demonstrate that the HOMO-LUMO band gap is narrowed in Cu/Ni-N-C, a feature that points to improved electronic conductivity and consequently higher catalytic activity potential, which stems from more efficient electron transfer throughout the reaction process (Fig. 5e and Fig. S38 in Supporting information). In addition, the introduction of Ni into the Cu-N-C matrix causes the D-band center of Cu 3d to positively shift from −3.396 eV to −2.844 eV (Fig. 5e), which infers stronger binding interactions with reaction intermediates. An analogous positive shift is also detected in the PDOS spectrum for the Ni 3d D-band center (Fig. S38).

The surface coverage of *H species over catalysts with distinct hybrid heterostructures was quantified by evaluating the free energy variations related to water dissociation (ΔG_{H_2O}) and hydrogen adsorption-desorption (ΔG_H) on Cu-N-C, Ni-N-C and Cu/Ni-N-C catalysts (Figs. 5f and g). Specifically, Cu/Ni-N-C exhibits a ΔG_{H_2O} value of 0.61 eV, which is considerably lower than those of Cu-N-C (1.65 eV) and Ni-N-C (1.20 eV) (Fig. 5f). This result manifests that the incorporation of Ni endows Cu/Ni-N-C with more thermodynamically favorable water dissociation kinetics, thus yielding an elevated *H concentration that is available for the subsequent electrocatalytic reactions. On the contrary, the absolute ΔG_H value of Cu/Ni-N-C is 1.08 eV, which is markedly lower than the corresponding values of Cu-N-C (1.96 eV) and Ni-N-C (1.86 eV) (Fig. 5g). To further clarify the CO formation mechanism over Cu/Ni-N-C, DFT calculations were utilized to simulate the Gibbs free energy profiles of the complete reaction sequence. As illustrated in Fig. 5h, the *COOH formation on Cu/Ni-N-C is energetically more favorable ($\Delta G = 1.78$ eV) than on Cu-N-C ($\Delta G = 2.52$ eV) and Ni-N-C ($\Delta G = 2.24$ eV). This suggests that Cu/Ni-N-C was more conducive to CO formation than the Cu-N-C and Ni-N-C catalysts. Furthermore, the thermodynamic barrier for *COOH formation is found to be higher on Cu-N-C ($\Delta G = 2.52$ eV) than on Ni-N-C ($\Delta G = 2.24$ eV), a result that verifies Ni (rather than Cu) as the preferred metal site for anchoring the C atom of *COOH moieties in Cu/Ni-N-C, which aligns with the findings in Fig. 5d.

To clarify the fundamental reason for this catalytic selectivity, we analyzed the structural configurations of the key *COOH intermediate on the surfaces of Cu-N-C, Ni-N-C and Cu/Ni-N-C catalysts (Fig. 5i). On Cu-N-C, the Cu-C bond length in the *COOH intermediate is 2.027 Å, and its C–OH bond length is 1.376 Å. In the same manner, the Ni-N-C surface exhibits a Ni-C bond length of 2.020 Å and a C–OH bond length of 1.360 Å for the adsorbed *COOH. In sharp contrast, the Cu/Ni-N-C surface shows a shortened Ni-C bond length of 1.921 Å for *COOH, as well as a corresponding C–OH bond length of 1.388 Å. Such structural changes are of great significance to the underlying reaction mechanism of CO_2RR. A longer C–OH bond on Cu/Ni-N-C points to a weaker interaction between C and O atoms, thus making the C–OH bond easier to break. On the other hand, the shorter Ni-C bond on Cu/Ni-N-C means a stronger binding between the metal site and carbon atom, which is more favorable for the formation of the *CO intermediate. This analysis of intermediate configurations offers a molecular-level interpretation for the improved *CO formation efficiency observed on the Cu/Ni-N-C catalyst, and these structural understandings also confirm the validity of our earlier energy calculations.

This study systematically investigates the structure and CO_2 electroreduction performance of Cu/Ni dual-atom catalysts (Cu/Ni-N-C) through a combination of experiments and theoretical calculations, clarifying the regulatory mechanism of intermetallic interactions on catalytic selectivity. Experimental results confirm that Cu and Ni atoms in Cu/Ni-N-C are each coordinated with four nitrogen atoms, forming uniformly distributed dual-atom active sites. The obtained Cu-N-C catalyst exhibits maximum FE_{CO} of 38.35 % at −1 V *vs.* RHE and maximum FE_{CH_4} of 21.89 % at −1.4 V *vs.* RHE, while the $Cu_{0.5}Ni_{0.5}$–N-C catalyst exhibits exceptional CO_2RR performance: At −1.3 V *vs.* RHE, the CO Faradaic efficiency (FE_{CO}) reaches 96.78 % with a partial current density of 24.80 mA/cm^2. The observed selectivity variation is caused by the electron-withdrawing effect of Ni atoms on Cu atoms in the Cu/Ni-N-C catalyst, which lowers the electron cloud density around Cu atoms and thus weakens the adsorption of CO_2RR intermediates on Cu sites. DFT calculations reveal the core mechanism underlying the enhanced catalytic performance for CO formation: Charge regulation between Cu and Ni forms an asymmetric adsorption mode. Electron-deficient Cu atoms act as O-terminal adsorption sites to bind the oxygen atoms of CO_2; while electron-enriched Ni atoms serve as C-terminal adsorption sites to anchor the carbon atoms. This synergistic adsorption promotes CO_2 polarization and activation, narrows the HOMO-LUMO band gap for efficient electron transfer, and reduces the thermodynamic barrier for *COOH intermediate formation. The Cu/Ni-N-C not only strengthens the binding between the metal site and carbon atom of CO_2 but also weakens the C–OH interaction, facilitating CO generation. This work provides new insights into the rational design of dual-atom catalysts and highlights the potential of regulating intermetallic interactions to optimize CO_2RR performance, advancing their industrial applications.

CRediT authorship contribution statement

Jielian Yang: Writing – original draft, Software, Formal analysis, Data curation. **Yue Shen:** Methodology, Investigation. **Bing Chen:** Methodology, Investigation. **Qi Wu:** Methodology, Investigation. **Yuemei Liao:** Methodology, Investigation. **Liya Zhou:** Writing – review & editing, Project administration, Funding acquisition. **Jing Luo:** Methodology, Investigation. **Xue Mao:** Methodology, Investigation. **Jin Guo:** Methodology, Investigation. **Binbin Luo:** Methodology, Investigation. **Qi Pang:** Methodology, Investigation.

Chunyan Zhou: Methodology, Investigation. **Peican Chen:** Writing – review & editing, Project administration, Funding acquisition. **Anxiang Guan:** Writing – review & editing, Resources, Project administration, Funding acquisition.

Declaration of competing interest

The authors declare that they have no known competing financial interests or personal relationships that could have appeared to influence the work reported in this paper.

Acknowledgments

We thank the following funding agencies for supporting this work: the Natural Science Foundation of Guangxi Province (No. 2025GXNSFBA069409), 2025 Annual Project for Improving the Basic Scientific Research Capabilities of Young and Middle-aged Teachers in Colleges and Universities of Guangxi (No. 2025KY0035), National Natural Science Foundation of China (No. 22465006); the Guangxi Science and Technology Major Program (No. Guike AA24263003); Guangxi Youth Talent Inclusive Support Policy Research Launch Fund (No. ZX02080030425009); the launch funding for high-level talent researchers of Guangxi University (No. ZX01080020124003).

Supplementary materials

Supplementary material associated with this article can be found, in the online version, at doi:10.1016/j.cclet.2026.112638.

References

[1] I. Song, Y. Eom, M. P, et al., Small 19 (2023) 2300049.
[2] F.M. Mota, D.H. Kim, Chem. Soc. Rev. 48 (2019) 205–259.
[3] Y. Birdja, E. Pérez-Gallent, M. Figueiredo, et al., Nat. Energy 4 (2019) 732–745.
[4] Y. Chen, X. Pan, L. Li, et al., Small 21 (2025) 2411249.
[5] G. Jeong, Y. Tan, J. Song, et al., Chem. Eng. J. 426 (2021) 131063.
[6] B. Chen, D. Shi, R. Deng, et al., ACS Catal. 14 (2024) 16224–16233.
[7] X. Zhang, X. Zhu, S. Bo, et al., Nat. Commun. 13 (2022) 5337.
[8] M. Hulsey, V. Fung, X. Hou, et al., Angew. Chem. Int. Ed. 61 (2022) e202208237.
[9] H. Fei, J. Dong, Y. Feng, et al., Nat. Catal. 1 (2018) 63–72.
[10] C. Xia, Y. Qiu, Y. Xia, et al., Nat. Chem. 13 (2021) 887–894.
[11] X. Liu, F. He, Y. Lu, et al., Chem. Eng. J. 453 (2023) 139833.
[12] J. Pei, H. Shang, J. Mao, et al., Nat. Commun. 15 (2024) 416.
[13] X. Niu, J. Wei, D. Xu, et al., Nano Res. 17 (2024) 4702–4710.
[14] J. Leverett, T. Tran-Phu, J. Yuwono, et al., Adv. Energy Mater. 12 (2022) 2201500.
[15] A. Guan, Y. Fan, S. Xi, et al., ACS Mater. Lett. 5 (2023) 19–26.
[16] D. Koshy, D. Chen, D. Lee, et al., Angew. Chem. Int. Ed. 59 (2020) 4043–4050.
[17] M. Fang, X. Wang, X. Li, et al., ChemCatChem 13 (2021) 603–609.
[18] S. Liang, J. Xiao, T. Zhang, et al., Angew. Chem. Int. Ed. 62 (2023) 202310740.
[19] X. Li, M. Qin, X. Wu, et al., Small 19 (2023) 2302530.
[20] S. Lu, M. Mazur, K. Guo, et al., Small 20 (2024) 2309251.
[21] X. Wang, N. Zhang, S. Guo, et al., J. Am. Chem. Soc. 146 (2024) 21357–21366.
[22] L. Zhang, N. Zhang, H. Shang, et al., Nat. Commun. 15 (2024) 9440.
[23] D. Yao, C. Tang, X. Zhi, et al., Adv. Mater. 35 (2023) 2209386.
[24] Y. Chen, J. Zhao, X. Pan, et al., Angew. Chem. Int. Ed. 63 (2024) e202411543.
[25] B. Hu, Y. Cao, Front. Energy. 19 (2025) 757–766.
[26] H. Xu, S. Fan, H. Liu, et al., Energy Storage Mater. 82 (2025) 104604.
[27] A. Guan, Z. Chen, Y. Quan, et al., ACS Energy Lett. 5 (2020) 1044–1053.
[28] L. Zhou, C. Yang, J. Wen, et al., J. Mater. Chem. A 5 (2017) 19343–19350.
[29] Y. Qian, P. Du, P. Wu, et al., J. Phys. Chem. C 120 (2016) 9884–9896.
[30] Z. Gu, N. Yang, P. Han, et al., Small Methods. 3 (2019) 1800449.
[31] H. Wang, H. Zou, Y. Liu, et al., Sci. Rep. 11 (2021) 21414.